RESEARCH ARTICLE

Check for updates

Achieving broadband ultraviolet to mid-infrared transparency in germanate-based nonlinear optical crystals Cs₃REGe₃O₉ (RE = Y, Gd)†

Jinmiao Jiao, Conggang Li, [ID] * Yuheng She, Ning Ye, Zhanggui Hu* and Yicheng Wu

Nonlinear optical (NLO) materials currently attract significant interest and hold paramount importance in the optoelectronic field. Nevertheless, the fabrication of NLO crystals capable of transmitting ultraviolet to mid-infrared wavelengths remains a formidable challenge. Herein, we synthesized two novel NLO crystals, namely Cs₃REGe₃O₉ (RE = Y, Gd), by employing a structural gene strategy that harmoniously merges flexible [YO₆] and [GdO₆] octahedra with rigid [GeO₄] motifs. Remarkably, Cs₃REGe₃O₉ (RE = Y, Gd) crystals exhibit substantial band gaps of 4.92 and 5.3 eV, respectively, while achieving the shortest reported ultraviolet cutoff edges at 210 and 215 nm among the boron-free germanate-based NLO materials. Importantly, these compounds also feature a remarkably broad infrared transparency range exceeding 6.8 μm. Furthermore, both compounds demonstrate a moderate second-harmonic-generation (SHG) response, comparable to that observed in KDP. Additionally, first-principles calculations unveil that the synergistic effect of the [REO₆] octahedra and [GeO₄] tetrahedra plays a pivotal role in governing the optical properties of Cs₃REGe₃O₉ (RE = Y, Gd). These explored findings offer a novel avenue for leveraging the highly desired NLO materials in the region spanning from ultraviolet to mid-infrared wavelengths.

Introduction

The exploration and fabrication of inorganic oxides exhibiting distinct optoelectronic attributes have garnered considerable recognition over recent decades.[1–4] Amongst these materials, those exhibiting acentric structures have assumed paramount significance in academic research and industrial applications due to their diverse functional attributes, including piezoelectricity, ferroelectricity, pyroelectricity, and nonlinear optical (NLO) properties.[5–10] The extensively employed NLO oxide compounds, such as borates including KBBF (KBe₂BO₃F₂),[11] β-BBO (β-BaB₂O₄),[12] LBO (LiB₃O₅),[13] CLBO(CsLiB₆O₁₀) crystals,[14] and phosphates including KDP (KH₂PO₄),[15] KTP (KTiOPO₄),[16] RTP (RbTiOPO₄),[17] *etc.*, have notably demonstrated their application in the spectral range, spanning from deep ultraviolet (UV) to near-infrared (IR). However, the rela-

tively elevated phonon energy inherent in these materials imposes a limitation on their capacity to fabricate NLO devices that operate beyond the wavelength threshold of 4.5 μm.[18]

In recent years, there has been a notable surge in scientific interest surrounding the pursuit of novel oxide crystals for mid-IR NLO applications. This endeavor involves the incorporation of heavy metal cations that are susceptible to second-order Jahn–Teller (SOJT) effects, and exemplary crystals include BaTeM₂O₉ (M = Mo, W),[19] Li₂MTeO₆ (M = Zr, Ti, Sn),[20,21] LiNbTeO₅,[22] Cs₂Bi₂OGe₂O₇,[23] Te₂V₂O₉,[24] and Cs₄V₈O₂₂.[25] As anticipated, these crystals exhibit an extended IR transmission cutoff edge beyond 5 μm. Unfortunately, the introduction of transition metal cations such as Bi³⁺, Ti⁴⁺, V⁵⁺, Nb⁵⁺, Mo⁶⁺, W⁶⁺, *etc.*, which participate second-order NLO processes, leads to an undesirable red shift of the UV cut-off edge, thereby impeding their suitability for utilization in the UV region. Consequently, the exploration into oxide NLO crystals capable of covering the transmission range from UV to mid-IR wavelengths remains a challenging task.

Based on previous investigations, germanate oxides have emerged as a highly promising and prospective prototype for the exploration of mid-IR NLO crystals, due to their structural diversity, including motifs such as [GeO₄], [Ge₂O₇], and [Ge₃O₉].[26,27] Moreover, the Ge–O bonds in germanate-based compounds possess a favorable low phonon energy, endowing

*Tianjin Key Laboratory of Functional Crystal Materials,
Institute of Functional Crystal, Tianjin University of Technology, Tianjin 300384,
China. E-mail: cgli@email.tjut.edu.cn, hu@mail.ipc.ac.cn*

This journal is © the Partner Organisations 2023

Inorg. Chem. Front., 2023, **10**, 6869–6878 | **6869**

them with an inherent extension of the transmission range in the IR region exceeding 6 μm. Compared with transition metal cations, rare earth cations demonstrate a versatile coordination with oxygen, thus facilitating the creation of acentric coordinated environments. Furthermore, rare earth cations, including Sc^{3+}, Y^{3+}, La^{3+}, Gd^{3+}, and Lu^{3+}, possess closed-shell electronic configurations or half-occupied 4f orbitals, which effectively eliminate d–d or f–f electronic transitions.[28] Consequently, this characteristic broadens the UV transparency window. Notable examples are observed in NLO-active rare earth borates such as $RECa_4O(BO_3)_3$ (RE = Y, Gd),[29] $K_5Mg_2La_3(BO_3)_6$,[30] and $K_7CdRE_2B_{15}O_{30}$ (RE = Sc, Y, Gd, Lu).[31] Therefore, to widen transmission range, it is speculated that the integration of rare earth cations exhibiting a conspicuous absence of d–d or f–f electron transitions, with germanates characterized by a diminished phonon energy, emerges as a promising avenue. This strategic approach not only preserves the distorted structural environments but also facilitates a favorable extension of the transmission range from UV to IR wavelengths.

Inspired above, we have successfully incorporated rare earth cations Y^{3+} and Gd^{3+} into germanates and extracted two novel NLO crystals, $Cs_3REGe_3O_9$ (RE = Y, Gd) (hereinafter designated as CYGO and CGGO), through spontaneous nucleation. The structure of $Cs_3GdGe_3O_9$ was initially documented in 2019,[32] yet hitherto, the investigation of its NLO properties and the correlation between its structure and properties has remained unexplored. Expectedly, these $Cs_3REGe_3O_9$ (RE = Y, Gd) crystals display an exceptionally wide transparency range. Notably, their ultraviolet cutoff edges, located at 210 and 215 nm respectively, represent the shortest UV wavelengths reported to date among the NLO boron-free germanates, while their IR cutoff edges extend beyond 6.8 μm. Moreover, these compounds feature good thermal stability and exhibit a moderate SHG activity, comparable to that of KDP. To gain deeper insights into the structure–property relationships of CYGO and CGGO, we performed comprehensive electronic structure analyses using density functional theory (DFT).

Experimental section

Synthesis and powder X-ray diffraction (PXRD)

The raw materials used in the experiments were all untreated: Cs_2CO_3 (Aladdin, 99.9%), Y_2O_3 (Aladdin, 99.9%), Gd_2O_3 (Aladdin, 99.9%), GeO_2 (Aladdin, 99.9%). CsF (Aladdin, 99.9%), Bi_2O_3 (Aladdin, 99.9%), PbO (Aladdin, 99.9%). The polycrystalline of $Cs_3REGe_3O_9$ (RE = Y, Gd) were synthesized utilizing the conventional high-temperature solid phase method. The raw materials were meticulously weighed according to specific stoichiometric ratios. Subsequently, the mixtures underwent thorough grinding and were preheated in a muffle furnace at 350 °C for a duration of 12 hours. Gradually, the temperature was heated up to 950 °C and sustained for a minimum of 48 hours, with intermittent grinding incorporated throughout the synthetic process. Room temperature

PXRD measurements were conducted on the polycrystalline powders of $Cs_3REGe_3O_9$ (RE = Y, Gd) using a SMartLab9 KW X-ray diffractometer. The measurements utilized a Cu-targeted K_α ray and encompassed a 2θ range spanning from 10–70°, with a set step size of 0.01° and a step time of 2 s.

Thermal properties

Thermogravimetric (TG) and differential scanning calorimetric (DSC) analyses were implemented on polycrystalline powders of the $Cs_3REGe_3O_9$ (RE = Y, Gd) compounds using a NETZSCH STA 449F5 thermoanalytical instrument. A limited quantity of samples was placed in a closed alumina crucible, which was heated up to 1200 °C at a heating rate of 10 °C min⁻¹ and then cooled to room temperature at the same rate under a nitrogen-protective atmosphere.

Crystal growth

Single crystals of $Cs_3REGe_3O_9$ (RE = Y, Gd) were extracted by the high temperature solution method. The polycrystalline materials and mixed fluxes $CsF–Bi_2O_3–PbO$ were placed in platinum crucibles and positioned within resistance furnaces. The temperature was gradually elevated to 900 °C and sustained for a duration of 12 hours to ensure the attainment of a uniform solution. Subsequently, the temperature was systematically reduced to 650 °C at a cooling rate of 3–5 °C per hour, followed by an additional descent to room temperature at a rate of 20 °C per hour. Ultimately, the $Cs_3REGe_3O_9$ (RE = Y, Gd) crystals were successfully obtained.

Structure determination

The single crystal X-ray diffraction analysis of CYGO and CGGO was executed on a Bruker SMART APEX II 4K CCD diffractometer. The diffraction experiments were carried out by employing Mo K_α radiation at a constant temperature of 297(2) K. The collected data were integrated using the SAINT program,[33] and the crystal structure was solved directly using the SHELXTL program,[34] which was used to improve the agreement between the calculated structure factors and the actual observations (Shelxt/XL), based on the full-matrix least squares method. The agreement between the calculated structure factors and the actual observations (Shelxt/XL) was used to determine the positions of the atoms in the initial structure, and the PLATON program was used to determine the structural alignment. Elaborated crystal parameters and refined structural data are comprehensively presented in the ESI,† including refined atomic positions, isotropic displacement parameters, bond lengths, and bond angles, documented in Tables S1–4.†

Energy-dispersive spectroscopy (EDS) measurements

The CYGO and CGGO samples were analyzed using a field emission scanning electron microscope equipped with energy dispersive X-ray spectrometry.

6870 | *Inorg. Chem. Front.*, 2023, **10**, 6869–6878

This journal is © the Partner Organisations 2023

Spectroscopy characterizations

The UV-vis-NIR diffuse reflectance spectra of the CYGO and CGGO samples were acquired at ambient temperature using a Hitachi UV-vis-NIR spectrophotometer, operating in the wavelength range of in the range 190–2000 nm, with barium sulfate as the reference sample. The IR spectra of the target samples were recorded employing a Nicolet iS50 FT-IR spectrometer. The recorded spectra encompassed wavelengths within the range of 400–4000 cm^{-1}.

Second harmonic generation (SHG) measurements

According to the method proposed by Kurtz and Perry,[35] the powder SHG responses of CYGO and CGGO were investigated by employing a Q-switch laser at the light source 1064 nm. The strength of the SHG response of a compound is contingent upon its particle size dimensions. To elucidate this relationship, the CYGO and CGGO samples were sieved into discrete particle size ranges: 53–75, 75–106, 106–120, 120–150, 150–180, and 180–212 μm. For the purpose of conducting a comparative analysis, KDP was employed as a reference sample within the identical particle size range.

Birefringence measurements

Birefringence, a pivotal characteristic of NLO materials, was assessed *via* the quartz wedge method, in accordance with the compensatory color principle. Regular crystals were employed in the visible range by using a Nikon Eclipse E200MV polarizing microscope. The experimental birefringence was quantified using the formula $R = |N_e - N_o| \times d = \Delta n \times d$, where Δn, R, and d represent the experimental birefringence, the optical range difference, and the corresponding thickness of the test crystal, respectively. The thickness of the selected CYGO and CGGO crystals was ascertained using a Bruker SMART APEX III CCD diffractometer. Also, based on the techniques provided by previous literature, we can deduce the color and order of interference exhibited by the crystals.[36]

Structure–prop-erty relationship

In order to elucidate the electronic structures and optical properties of CYGO and CGGO, we employed the CASTEP package,[37] which is grounded in the principles of density functional theory (DFT).[38] To achieve this, the crystal structures of CYGO and CGGO were optimized by employing the Perdew–Burke–Ernzerhof (PBE) exchange–correlation functional, bolstered by the generalized gradient approximation (GGA).[39] In the calculations, we assigned Cs $5s^25p^66s^1$, Y $4d^15s^2$, Gd $5d^16s^2$, Ge $4s^24p^2$, and O $2s^22p^4$ as the valence electrons for the respective atoms in CYGO and CGGO. The theoretical calculations were conducted with the aid of experimental single-crystal structural data for CYGO and CGGO. The kinetic energy cutoff (810 eV) and Monkhorst–Pack k-point meshes ($3 \times 6 \times 3$) were employed to ensure the adequate accuracy of the simulated results.

Results and discussion

Synthesis and thermal properties

The polycrystalline samples of CYGO and CGGO were obtained by a high-temperature solid phase reaction process. Fig. 1a and b evidently illustrates that the experimental PXRD patterns of CYGO and CGGO are in good agreement with those observed in theoretical results, thereby attesting to their high purity. Furthermore, DSC thermal analysis conducted over a temperature range of 40–1200 °C revealed a conspicuous absence of absorption peaks in both CYGO and CGGO as presented in Fig. 1c and d. Meanwhile, the corresponding TG curves exhibited negligible weight loss, underscoring the extraordinary thermodynamic stability of CYGO and CGGO, which surpasses 1200 °C. Furthermore, the examinations of CYGO and CGGO were carried out through a variable temperature XRD analysis, spanning a temperature range of 950–1300 °C, as depicted in Fig. 1e and f. Notably, the XRD patterns of both compounds exhibited stability until reaching a temperature threshold of 1250 °C, which further validates the soundness of the thermal analyses. An in-depth analysis of the PXRD spectra of the CYGO and CGGO samples after calcination at 1250 °C (Fig. S1†), thus substantiating that these two target compounds possess a distinctive incongruent melting behavior.

Structural analyses

CYGO and CGGO crystals were cultivated through the high-temperature solution method utilizing mixed fluxes CsF–Bi_2O_3–PbO. Small crystals of regular shape and high quality are selected for single crystal measurements analysis. The structure of CGGO was initially reported in 2019.[32] To investigate the correlation between structure and performance, its crystal structure was reconfirmed. The detailed crystallographic data, along with the corresponding experimental condition are given in Table 1. It was ascertained that CYGO and CGGO are isomorphic, crystallizing in the orthorhombic space group $Pna2_1$ (no. 33). The unit cell parameters for these two crystals determined as follows: $a = 13.7994(3)$ Å, $b = 7.1087(2)$ Å, $c = 12.7190(3)$ Å and $Z = 4$ for CYGO; and $a = 13.908(3)$ Å, $b = 7.1769(17)$ Å, $c = 12.8026(5)$ Å and $Z = 4$ for CGGO, respectively. Since the structures of these two compounds exhibit isomorphism, the as-synthesized CYGO was selected as the representative to expound upon their structural characteristics. The asymmetric unit of CYGO comprises one crystallographically independent Y site, three Ge sites, three crystallographically distinct Cs sites, and nine oxygen sites. As depicted in Fig. 2a, each Y^{3+} cation is ligand linked to six oxygen atoms, forming distortive octahedra $[YO_6]$, with the Y–O bond lengths varying within the range of 2.241(6)–2.281(6) Å. A Ge^{4+} cation is coordinated with four oxygen atoms, resulting in the formation of tetrahedra $[GeO_4]$, characterized by bond lengths ranging from 1.712(6) to 1.789(6) Å. Notably, the adjacent $[GeO_4]$ tetrahedra are interconnected with each other to form $[Ge_6O_{19}]$ short zigzag chains, which extend infinitely along the c-axis (Fig. 2b). The separated $[YO_6]$ octahedra are evenly distributed throughout the structural space and play a connecting role. As
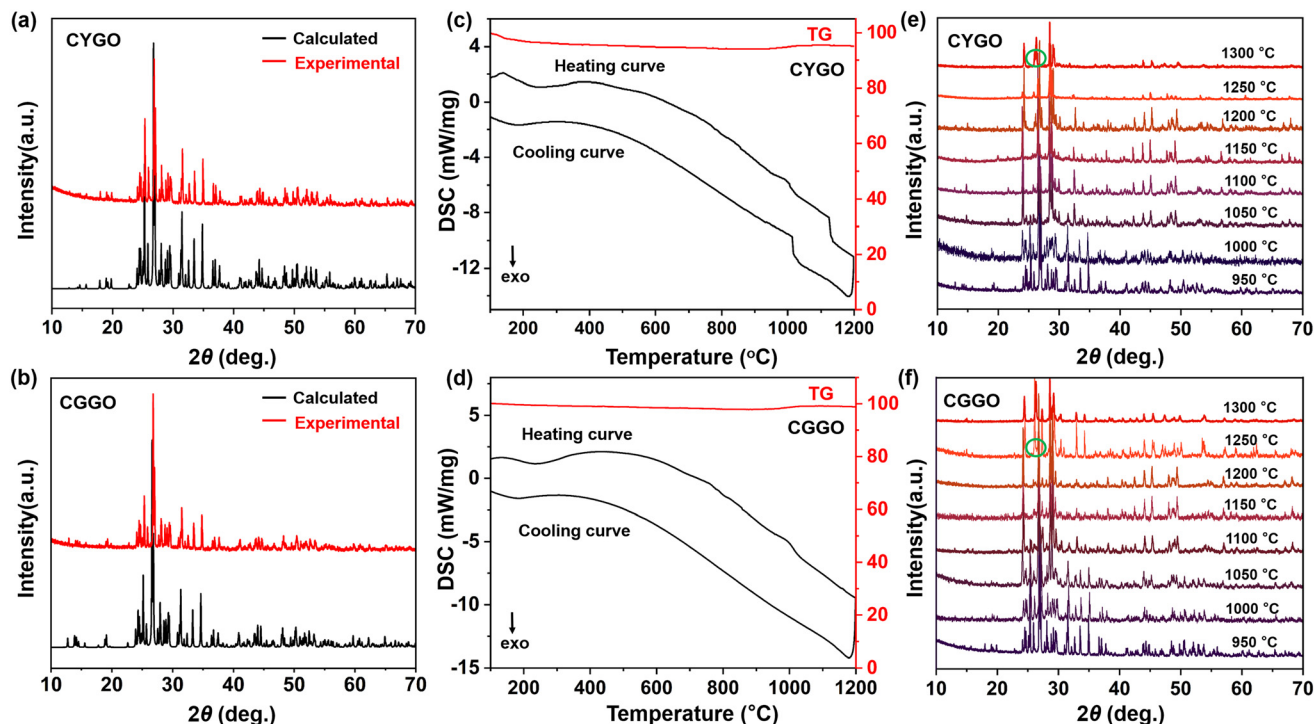
Fig. 1 (a and b) Experimental and theoretical PXRD patterns of CYGO and CGGO; (c and d) TG-DSC curves of CYGO and CGGO; (e and f) the PXRD patterns evolution of CYGO and CGGO polycrystalline pure phases under elevated temperature conditions.

Table 1 Crystal data and structure refinements for CYGO and CGGO

Empirical formula	$Cs_3YGe_3O_9$	$Cs_3GdGe_3O_9$
Formula weight	849.41	917.75
Crystal system	Orthorhombic	Orthorhombic
Space group	$Pna2_1$	$Pna2_1$
a (Å)	13.7994(3)	13.908(3)
b (Å)	7.1087(2)	7.1769(17)
c (Å)	12.7190(3)	12.826(3)
Volume (Å^3)	1247.68(5)	1280.3(5)
Z	4	4
Density (g cm^{-3})	4.522	4.761
Crystal size (mm^3)	0.074 × 0.050 × 0.038	0.19 × 0.07 × 0.06
Completeness	100%	100%
R (int)	0.033	0.072
GOF on (F^2)	1.065	1.112
Final R indices	$R_1 = 0.0290$,	$R_1 = 0.0505$,
$[I > 2\sigma(I)]^a$	$wR_2 = 0.0646$	$wR_2 = 0.1281$
R indices (all data)	$R_1 = 0.0322$,	$R_1 = 0.0530$,
	$wR_2 = 0.0663$	$wR_2 = 0.1299$
CCDC number	2293196	2293197

$^a R_1 = \sum ||F_o| - |F_c||/\sum |F_o|$; $wR_2 = [\sum w(F_o^2 - F_c^2)^2/\sum w(F_o^2)^2]^{1/2}$.

clearly illustrated in Fig. 2c, the neighboring $[Ge_6O_{19}]_\infty$ zigzag chains are interconnected by the $[YO_6]$ octahedra, giving rise to quasi-planar structures. Subsequently, these quasi-planes further interconnect to construct a three-dimensional (3D) framework (Fig. 2d). All the Cs atoms occupy the voids to maintain charge balance.

To validate the rationality of the structural analysis, the bond valences of various atoms in CYGO and CGGO were calculated. The resulting valence states for the elements Y/Gd,

Ge, Cs, and O were determined to be 3.11/3.15, 3.95–4/3.79–4.06, 0.81–1/0.77–1.27, and 1.89–2.06/1.80–2.17, respectively, which agree well with those derived from the structural data. Additionally, the elemental compositions and mapping of these two compounds were analyzed through EDS measurements as presented in Fig. S2 and 3.† The ratios of Cs/Y/Ge/O in CYGO and Cs/Gd/Ge/O in CGGO are found to be 3.3/1/2.8/11.6, and 3.1/1/3.2/12.9, respectively. These observations align remarkably well with the atomic molar ratio of their structures, providing further evidence for the rationality of the proposed structure.

Spectroscopy characterizations

The UV-vis-NIR spectrum of the CYGO and CGGO compounds are deposited in Fig. 3a and b. It's worth noteworthy that both CYGO and CGGO exhibit remarkable UV cut-off edges at 210 nm and 215 nm, respectively, accompanied by wide band gaps of 4.92 and 5.3 eV, as determined through the Kubelka–Munk formula.[40] Comparisons made as in Fig. 3e, to the best of our knowledge, these UV cut-off edges represent the shortest reported among boron-free germanate-based NLO crystals. Moreover, the IR spectrum analyses, illustrated in Fig. 3c and d, reveal the absence of conspicuous absorption within a broad range of 3500–731 cm^{-1} for both CYGO and CGGO. Accordingly, these two crystals demonstrate transparency cover a wide spectral range spanning 3–6.8 μm, as determined by the two-phonon approximation, thereby presenting a favorable prospect for mid-IR NLO applications. The specific vibrational
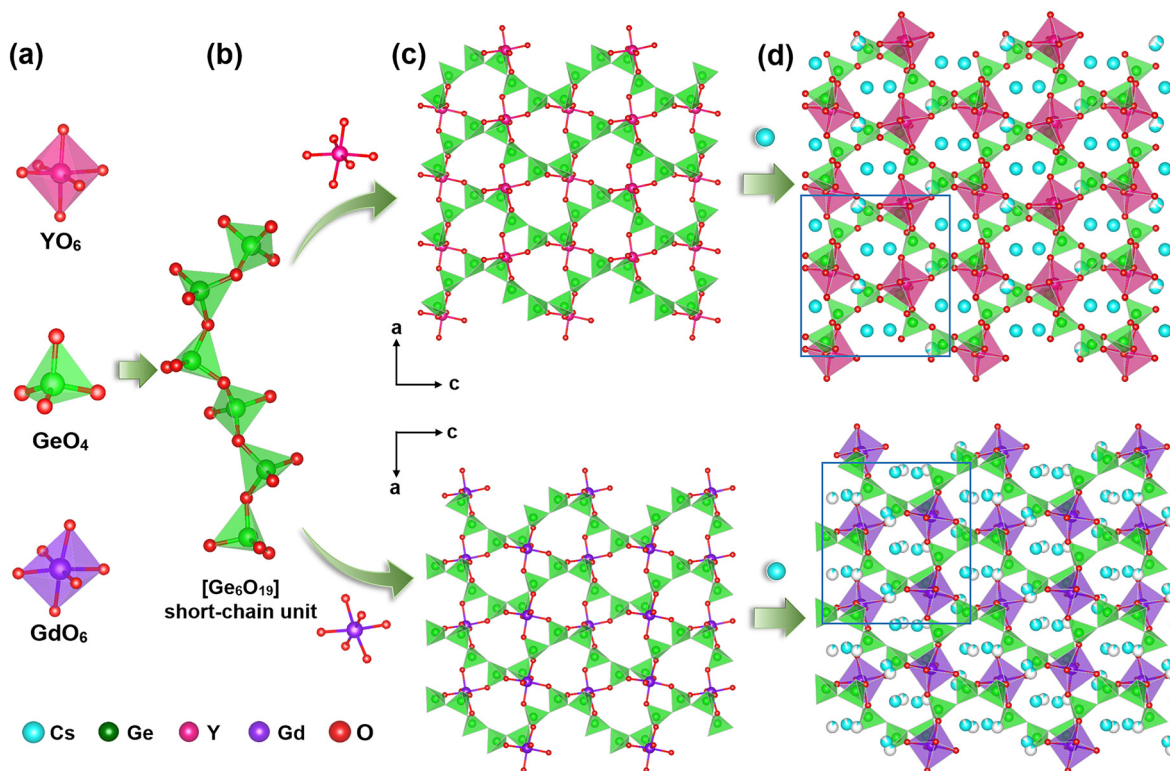
6872 | *Inorg. Chem. Front.*, 2023, **10**, 6869–6878

This journal is © the Partner Organisations 2023

Fig. 2 (a) Structural motifs [Ge₄], [YO₆], [GdO₆] of Cs₃REGe₃O₉; (b) [Ge₆O₁₉] short-chain unit; (c) quasi-planar structures of Cs₃REGe₃O₉ paralleled to the *ac* plane, and (d) 3D framework structure of Cs₃REGe₃O₉.
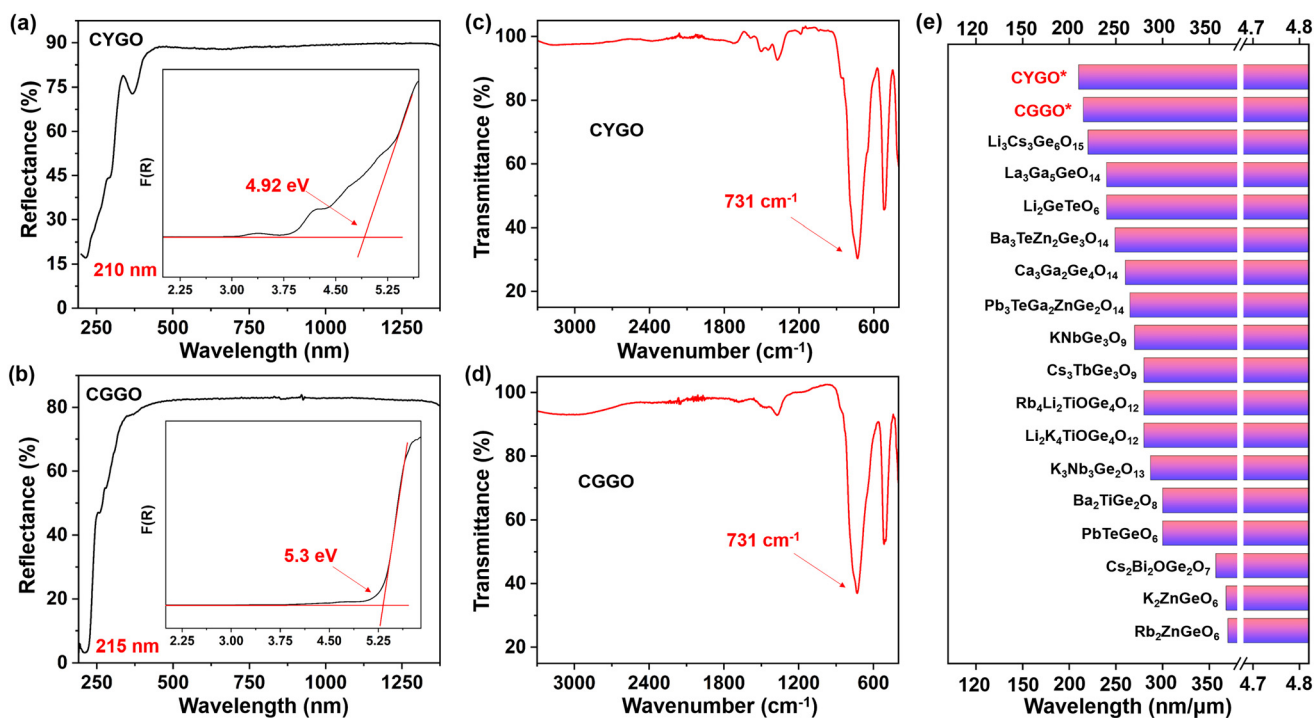

Fig. 3 (a and b) UV-vis-NIR diffuse reflectance spectra of the CYGO and CGGO, respectively; (c and d) IR spectrum of the CYGO and CGGO, respectively; (e) comparison of the UV cutoff edge among the boron-free germanate-based NLO crystals (* refers to compounds derived from this work).

This journal is © the Partner Organisations 2023

Inorg. Chem. Front., 2023, **10**, 6869–6878 | **6873**

modes of the infrared absorption peaks are shown in Table S5.† Based on the aforementioned observations, it becomes apparent that the transmission range of both crystals almost covers the pivotal solar-blind region, along with the 3–5 μm mid-IR atmospheric transmission window. These findings strongly suggest the potential suitability of these crystals as NLO materials in a wide transmission window from UV to mid-IR wavelengths. A comprehensive comparison of the band gap and UV cut-off of various boron-free germanate-based NLO materials is presented in Table 2.

Second-harmonic generation measurement

As CYGO and CGGO crystallize into the non-centrosymmetric (NCS) structure, powder SHG measurements were conducted employing KDP samples as a reference, following the well-established Kurtz–Perry method. As depicted in Fig. 4a and b, the SHG intensities of CYGO and CGGO demonstrate a progressive enhancement as the particle size of the polycrystalline powder increases, ultimately attaining saturation. This phenomenon unequivocally signifies their inherent phase matching behavior. Furthermore, within the particle size range of 180–212 μm, CYGO and CGGO exhibit commendable SHG intensities, approximating that of 0.7 × KDP. Also, the SHG performance of CYGO and CGGO is compared to many other germanate-based oxide crystals, such as Rb_2ZnGeO_6 and K_2ZnGeO_6.

Birefringence properties

The experimental determination of birefringence values for CYGO and CGGO was performed through the utilization of the quartz wedge method. As illustrated in Fig. 5a–f, the thickness of these examined crystals was discerned to be 26.3 and 18.3 μm, respectively. The optical path difference of the $Cs_3REGe_3O_9$ (RE = Y, Gd) crystals was found to be 489 and 442 nm, respectively, under visible light wavelength. An initial
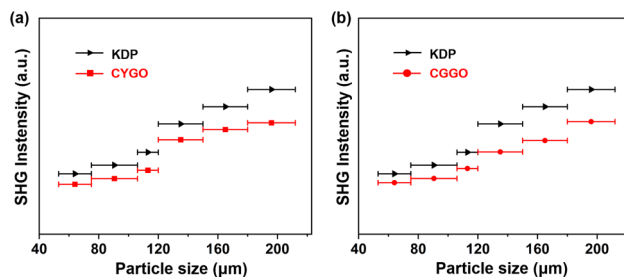

Fig. 4 (a and b) The phase-matched patterns and SHG intensity of CYGO and CGGO with the practical KDP as a reference, respectively.

first-order orange hue was ascertained through the control Michal-Levy interferometric chromatogram. Employing the birefringence formula $R = |N_e - N_o| \times d = \Delta n \times d$, the visible region yielded experimental birefringence values of 0.0186 and 0.0241 for CYGO and CGGO, respectively. These birefringent tendencies exhibited by CYGO and CGGO align favorably with those of other germanate-based crystals, such as Rb_2ZnGeO_6 (0.019 @ 1 μm), $Y_2Ge_2O_7$ (0.028 @1064 μm)[44] and K_2ZnGeO_6 (0.017 @1064 μm),[42] $Li_2Ge_7O_{15}$ (0.018 @1064 μm).

Theoretical calculations

To unravel the underlying optical origin of the target compounds, an analysis of the electronic structure was performed *via* first-principles calculations. Given the isomorphic nature of the crystal structures of CYGO and CGGO, CYGO was selected as the representative for conducting the theoretical examination. As delineated in Fig. 6a, the apex of the valence band manifests at the X position, while the lowest point of the conduction band emerges at the G position, signifying CYGO to be an indirect band gap compound with a gap width of 4.9 eV. Additionally, as depicted in Fig. 6b, the density of states reveals that the energy range of −5 to 0 eV is largely consti-

Table 2 Comparison of the UV cutoff edge among the boron-free germanate-based NLO crystals

Compounds	Crystal system	Space group	Bandgap (eV)	UV cut-off (nm)	Structural units
Rb_2ZnGeO_6 [41]	Orthorhombic	$C222_1$	3.22	370	$GeO_4 + ZnO_4$
K_2ZnGeO_6 [42]	Orthorhombic	$C222_1$	3.23	368	$GeO_4 + ZnO_4$
$Cs_2Bi_2O(Ge_2O_7)$ [23]	Orthorhombic	$Pca2_1$	3.15	357	$Bi_2O_8 + Ge_2O_7$
$PbTeGeO_6$ [43]	Trigonal	$P31m$	3.36	300	$Te/GeO_6 + PbO_6$
$Ba_2TiGe_2O_8$ [44]	Orthorhombic	$Cmm2$	3.14	300	$Ge_2O_7 + TiO_5$
$K_3Nb_3Ge_2O_{13}$ [45]	Hexagonal	$P\bar{6}c2$	3.75	287	$Ge_2O_7 + Nb_3O_{15}$
$Li_2K_4TiOGe_4O_{12}$ [46]	Tetragonal	$P4nc$	4.43	280	$TiO_5 + GeO_4$
$Rb_4Li_2TiOGe_4O_{12}$ [47]	Tetragonal	$P4nc$	N/A	280	$TiO_5 + GeO_4$
$Cs_3TbGe_3O_9$ [39]	Orthorhombic	$Pna2_1$	3.4	280	$GeO_4 + TbO_6$
$KNbGe_3O_9$ [45]	Hexagonal	$P\bar{6}2c$	4.59	270	$Ge_3O_9 + NbO_6$
$Pb_3TeGa_2ZnGe_2O_{14}$ [48]	Trigonal	$P321$	4.67	265	$GeO_4 + Ga/ZnO_4 + TeO_6 + PbO_8$
$Ca_3Ga_2Ge_4O_{14}$ [44]	Trigonal	$P321$	N/A	260	$GeO_4 + GeO_6 + GaO_4$
$Ba_3TeZn_2Ge_3O_{14}$ [49]	Trigonal	$P321$	3.98	249	$GeO_4 + ZnO_4 + TeO_6 + PbO_8$
Li_2GeTeO_6 [50]	Trigonal	$R3$	4.65	240	$GeO_6 + TeO_6$
$La_3Ga_5GeO_{14}$ [44]	Trigonal	$P321$	N/A	240	$GeO_4 + LaO_8 + GaO_6 + GaO_4$
$Li_3Cs_3Ge_6O_{15}$ [51]	Orthorhombic	$Pca2_1$	3.23	220	GeO_4
CGGO this work	Orthorhombic	$Pna2_1$	5.1	215	$GeO_4 + GdO_6$
CYGO this work	Orthorhombic	$Pna2_1$	4.82	210	$GeO_4 + YO_6$

N/A: not reported or unavailable.

6874 | *Inorg. Chem. Front.*, 2023, **10**, 6869–6878

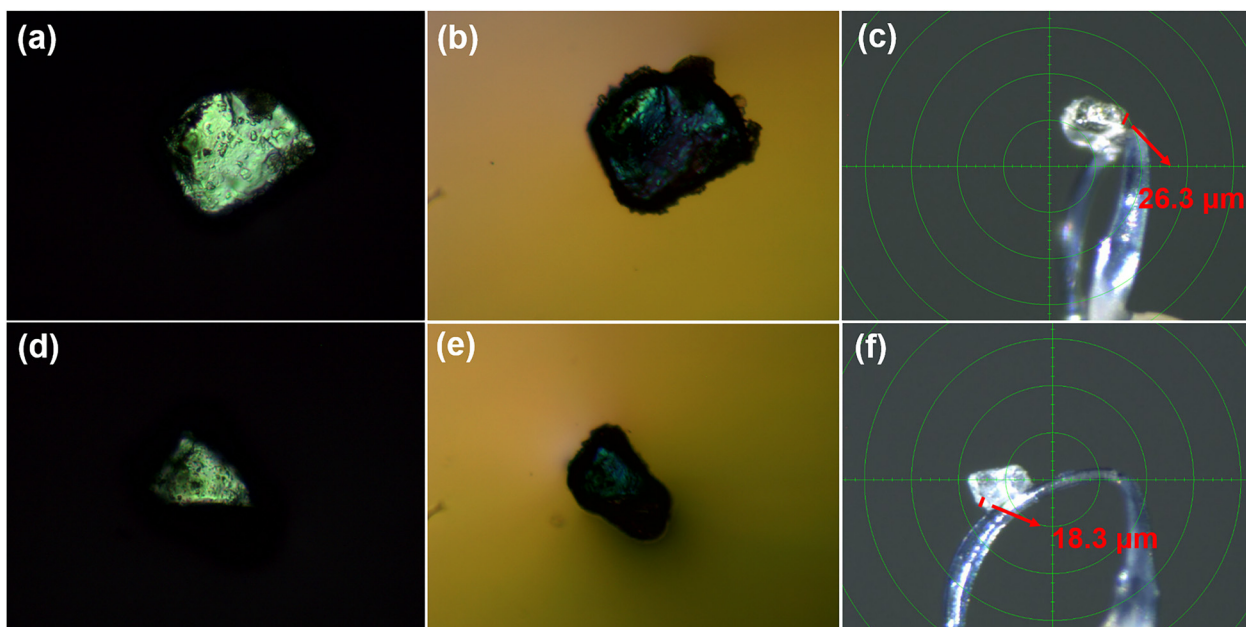This journal is © the Partner Organisations 2023

Fig. 5 (a–c) The original interference color, extinction and thickness of the CYGO crystal, respectively; (d–f) the original interference color, extinction and thickness of the CGGO crystal, respectively.
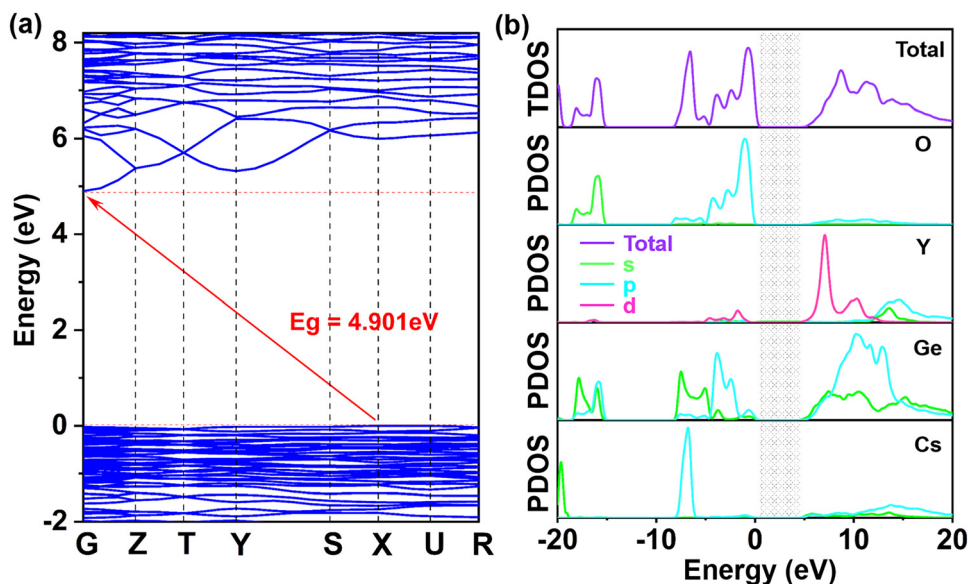

Fig. 6 (a) The bandgap structure of CYGO; (b) the TDOS and PDOS of CYGO.

tuted by Y 4d, Ge 4s 4p, and O 2p orbitals. Likewise, the Cs 5p and O 2p orbitals account for the states spanning −10 to −5 eV, while the energy range of 10–15 eV is predominantly attributable to Ge 4s 4p and O 2s 2p orbitals. Considering that electronic states proximate to the Fermi level wield considerable influence over the optical properties of compounds, it can be concluded that the $[YO_6]$ and $[GeO_4]$ units play pivotal roles in the NLO and birefringent characteristics of the CYGO crystal.

Conclusions

In summary, by employing the structural gene engineering, we have cultivated two novel NLO germinate-based crystals, $Cs_3REGe_3O_9$ (RE = Y, Gd) using a flux method. These compounds exhibit structural isomorphism, forming a 3D framework composed of $[YO_6]/[GdO_6]$ octahedra and $[GeO_4]$ tetrahedra. Notably, $Cs_3REGe_3O_9$ (RE = Y, Gd) possesses the shortest UV cutoff edges among boron-free germinate-based NLO

This journal is © the Partner Organisations 2023

Inorg. Chem. Front., 2023, **10**, 6869–6878 | **6875**

materials, with values of 210 nm and 215 nm, respectively. Remarkably, IR analyses revealed that these crystals display expansive transmission regions extending beyond 6.8 μm. Moreover, $Cs_3REGe_3O_9$ (RE = Y, Gd) exhibit a moderate SHG intensity, comparable to that of KDP. Additionally, theoretical analyses have elucidated the pivotal role played by the $[YO_6]$/$[GdO_6]$ and $[GeO_4]$ units in governing the observed NLO and birefringent properties of $Cs_3REGe_3O_9$ (RE = Y, Gd). With these favorable attributes, $Cs_3REGe_3O_9$ (RE = Y, Gd) emerge as prospective contenders for NLO applications spanning the UV to IR region., thereby forging a path toward the exploration of novel NLO crystals endowed with a broad transmission window.

Conflicts of interest

There are no conflicts to declare.

Acknowledgements

References

1 P. S. Halasyamani and K. R. Poeppelmeier, Noncentro symmetric Oxides, *Chem. Mater.*, 1998, **10**, 2753–2769.

2 (*a*) C. Chen, Y. C. Wu and R. Li, The anionic group theory of the nonlinear optical effect and its applications in the development of new high-quality NLO crystals in the borate series, *Int. Rev. Phys. Chem.*, 1988, **8**, 65–91; (*b*) M. Mutailipu, F. Li, C. Jin, Z. Yang, K. R. Poeppelmeier and S. Pan, Strong nonlinearity induced by coaxial alignment of polar chain and Dense $[BO_3]$ Units in $CaZn_2(BO_3)_2$, *Angew. Chem., Int. Ed.*, 2022, **61**, e202202096.

3 A. Tudi, S. Han, Z. Yang and S. Pan, Potential optical functional crystals with large birefringence: Recent advances and future prospects, *Coord. Chem. Rev.*, 2022, **459**, 214380.

4 A. Tudi, C. W. Xie, S. L. Pan and Z. H. Yang, Design of novel DUV nonlinear optical materials with one-dimensional functional module $[BO_2]_\infty$ chain by fluorine-driven short phase-matching, *Mater. Today Phys.*, 2022, **28**, 100852.

5 T. Zheng, Q. Wang, J. X. Ren, L. L. Cao, L. Huang, D. J. Gao, J. Bi and G. H. Zou, Halogen regulation triggers structural transformation from centrosymmetric to noncentrosymmetric switches in tin phosphate halides Sn_2PO_4X (X = F, Cl), *Inorg. Chem. Front.*, 2022, **9**, 4705–4713.

6 H. Y. Sha, J. X. Xu, Z. Y. Xiong, Z. J. Wang, R. B. Su, C. He, X. M. Yang, X. F. Long and Y. Liu, An optimized $KBe_2BO_3F_2$-Like structure: The unity of Deep-ultraviolet

7 Y. H. She, F. Liang, J. M. Jiao, W. L. Zhao, N. Ye, Z. G. Hu, Y. C. Wu and C. G. Li, A new stable polymorph of $Li_2TeMo_3O_{12}$ with wide mid-infrared transparency and a large Raman response, *Inorg. Chem. Front.*, 2023, **10**, 3595–3604.

8 L. Kang and Z. S. Lin, Deep-ultraviolet nonlinear optical crystals: concept development and materials discovery, *Light: Sci. Appl.*, 2022, **11**, 201–213.

9 J. Wang, B. Xiong, H. Wu, H. Yu, Z. Hu, J. Wang and Y. Wu, $Bi_{32}Cd_3P_{10}O_{76}$: a new congruently melting nonlinear optical crystal with a large SHG response and a wide transparent region, *Inorg. Chem. Front.*, 2021, **8**, 344–351.

10 W. Zhao, C. Li, T. Han, J. Jiao, Y. She, D. Ju, F. Liang, N. Ye, Z. Hu and Y. Wu, $Cs_2Bi_2OSi_2O_7$: A promising bismuth silicate nonlinear optical crystal with face-sharing BiO_5 Polyhedra exhibiting strengthened second harmonic generation response and birefringence, *Chem. Mater.*, 2022, **34**, 3365–3372.

11 C. Chen, T. Sasaki, R. Li, Y. Wu, Z. Lin, Y. Mori, Z. Hu, J. Wang, S. Uda, M. Yoshimura and Y. S. Kaneda, *Nonlinear optical borate crystals: Principles and applications*, Wiley-VCH Verlag GmbH & Co. KGaA, Weinheim, Germany, 2012.

12 C. Chen, Y. Wang, Y. Xia, B. Wu, D. Tang, K. Wu, W. Zeng, L. Yu and L. Mei, New development of nonlinear optical crystals for the ultraviolet region with molecular engineering approach, *J. Appl. Phys.*, 1995, **77**, 2268–2272.

13 C. Chen, Y. Wu, A. Jiang, B. Wu, G. You, R. Li and S. Lin, New nonlinear-optical crystal: LiB_3O_5, *J. Opt. Soc. Am. B*, 1989, **6**, 616–621.

14 T. Sasaki, Y. Mori and M. Yoshimura, Progress in the growth of a $CsLiB_6O_{10}$ crystal and its application to ultraviolet light generation, *Opt. Mater.*, 2003, **23**, 343–351.

15 D. Wang, T. Li, S. Wang, J. Wang, Z. Wang, X. Xu and F. Zhang, Study on nonlinear refractive properties of KDP and DKDP crystals, *RSC Adv.*, 2016, **6**, 14490–14495.

16 R. A. Stolzenberger, Nonlinear optical properties of flux growth $KTiOPO_4$, *Appl. Opt.*, 1988, **27**, 3883–3886.

17 Yu. S. Oseledchik, A. I. Pisarevsky, A. L. Prosvirnin, V. V. Starshenko and N. V. Svitanko, Nonlinear optical properties of the flux grown $RbTiOPO_4$ crystal, *Opt. Mater.*, 1994, **3**, 237–242.

18 C. Yang, X. Liu, C. L. Teng, X. H. Cheng, F. Liang and Q. Wu, Hierarchical molecular design of high-performance infrared nonlinear Ag_2HgI_4 material by defect engineering strategy, *Mater. Today Phys.*, 2021, **19**, 100432–100439.

19 H. S. Ra, K. M. Ok and P. S. Halasyamani, Combining second order Jahn-Teller distorted cations to create highly efficient SHG materials: synthesis, characterization, and NLO properties of $BaTeM_2O_9(M = Mo^{6+}$ or $W^{6+})$, *J. Am. Chem. Soc.*, 2003, **125**, 7764–7765.

20 W. Q. Lu, Z. L. Gao, X. T. Liu, X. X. Tian, Q. Wu, C. G. Li, Y. X. Sun, Y. Liu and X. T. Tao, Rational design of a $LiNbO_3$-like nonlinear optical crystal, Li_2ZrTeO_6, with high

6876 | *Inorg. Chem. Front.*, 2023, **10**, 6869–6878

This journal is © the Partner Organisations 2023

laser-damage threshold and wide mid-IR transparency window, *J. Am. Chem. Soc.*, 2018, **140**, 13089–13096.

21 X. Du, X. Guo, Z. Gao, F. Liu, F. Guo, S. Wang, H. Wang, Y. Sun and X. Tao, Li_2MTeO_6 (M = Ti, Sn): Mid-infrared nonlinear optical crystal with strong second harmonic generation response and wide transparency range, *Angew. Chem., Int. Ed.*, 2021, **60**, 23320–23326.

22 K. Chen, C. Lin, G. Peng, Y. Chen, H. Huang, E. Chen, Y. Min, T. Yan, M. Luo and N. Ye, $LiNbTeO_5$: A high-performance multifunctional crystal material with a very large second-harmonic generation response and piezoelectric coefficient, *Chem. Mater.*, 2021, **34**, 399–404.

23 R. L. Tang, C. L. Hu, B. L. Wu, Z. Fang, Y. Chen and J. G. Mao, $Cs_2Bi_2O(Ge_2O_7)$ (CBGO): A larger SHG effect induced by synergistic polarizations of BiO_5 polyhedra and GeO_4 tetrahedra, *Angew. Chem.*, 2019, **131**, 15502–15505.

24 S. P. P. Sadhu, T. Shet, B. K. Abhijit, A. Pradhan, M. Molli, V. Sai Muthukumar and K. B. R. Varma, Linear and nonlinear optical properties of Tellurium Vanadate ($Te_2V_2O_9$), *Opt. Mater.*, 2017, **69**, 128–133.

25 C. Wu, X. X. Jiang, L. Lin, Y. L. Hu, T. H. Wu, Z. S. Lin, Z. P. Huang, M. G. Humphrey and C. Zhang, A congruent-melting mid-infrared nonlinear optical vanadate exhibiting strong second-harmonic generation, *Angew. Chem.*, 2021, **133**, 22621–22627.

26 F. Dal Bo, S. M. Aksenov and P. C. Burns, A novel family of microporous uranyl germanates: Framework topology and complexity of the crystal structures, *J. Solid State Chem.*, 2019, **271**, 126–134.

27 Z. E. Lin and G. Y. Yang, Germanate frameworks constructed from oxo germanium cluster building units, *Eur. J. Inorg. Chem.*, 2010, **2010**, 2895–2902.

28 J. Zhao, D. J. Mei, W. K. Wang, Y. D. Wu and D. F. Xue, Recent advances in nonlinear optical rare earth structures, *J. Rare Earths*, 2021, **39**, 1455–1466.

29 M. Iwai, T. Kobayashi, H. Furuya, Y. Mori and T. Sasaki, Crystal growth and optical characterization of rare-earth (Re) calcium oxyborate $ReCa_4O(BO_3)_3$ (Re = Y or Gd) as new nonlinear optical material, *J. Appl. Phys.*, 1997, **36**, L276–L279.

30 R. Liu, H. Wu, H. Yu, Z. Hu, J. Wang and Y. Wu, $K_5Mg_2La_3(BO_3)_6$: An efficient, deep-ultraviolet nonlinear optical material, *Chem. Mater.*, 2021, **33**, 4240–4246.

31 Z. Q. Xie, M. Mutailipu, G. J. He, G. P. Han, Y. Wang, Z. H. Yang, M. Zhang and S. L. Pan, A series of rare-earth borates $K_7MRE_2B_{15}O_{30}$ (M = Zn, Cd, Pb; RE = Sc, Y, Gd, Lu) with large second harmonic generation responses, *Chem. Mater.*, 2018, **30**, 2414–2423.

32 G. Morrison, N. R. Spagnuolo, S. G. Karakalos and H. C. zur Loye, $Cs_3RE^{III}Ge_3O_9$ (RE = Pr, Nd, and Sm-Yb) and $Cs_8Tb^{III}_2TbIVGe_9O_{27}$: A rare example of a mixed-valent Tb(III)/Tb(IV) oxide, *Inorg. Chem.*, 2019, **58**, 8702–8709.

33 W. Zhang, J. Sun, X. Wang, G. Shen and D. Shen, Crystal growth and optical properties of a noncentrosymmetric molybdenum tellurite, $Na_2Te_3Mo_3O_{16}$, *CrystEngComm*, 2012, **14**, 3490–3494.

34 G. M. Sheldrick, A short history of SHELX, *Acta Crystallogr., Sect. A*, 2008, **64**, 112–122.

35 S. K. Kurtz and T. T. Perry, A powder technique for the evaluation of nonlinear optical materials, *J. Appl. Phys.*, 1968, **39**, 3798–3813.

36 W. Huang, X. Zhang, Y. Li, Y. Zhou, X. Chen, X. Li, F. Wu, M. Hong, J. Luo and S. Zhao, A hybrid halide perovskite birefringent crystal, *Angew. Chem., Int. Ed.*, 2022, **61**, e202202746.

37 J. P. Perdew, A. Ruzsinszky, G. I. Csonka, O. A. Vydrov, G. E. Scuseria, L. A. Constantin, X. Zhou and K. Burke, Restoring the density-gradient expansion for exchange in solids and surfaces, *Phys. Rev. Lett.*, 2008, **100**, 136406.

38 V. Milman, K. Refson, S. J. Clark, C. J. Pickard, J. R. Yates, S. P. Gao, P. J. Hasnip, M. I. J. Probert, A. Perlov and M. D. Segall, Electron and vibrational spectroscopies using DFT, plane waves and pseudopotentials: CASTEP implementation, *J. Mol. Struct.: THEOCHEM*, 2010, **954**, 22–35.

39 A. M. Rappe, K. M. Rabe, E. Kaxiras and J. D. Joannopoulos, Optimized pseudopotentials, *Phys. Rev. B: Condens. Matter Mater. Phys.*, 1990, **41**, 1227–1230.

40 J. Tauc, Absorption Edge and Internal Electric Fields in Amorphous Semiconductors, *Mater. Res. Bull.*, 1970, **5**, 721–729.

41 T. Han, C. Li, W. Zhao, Y. She, J. Jiao, F. Liang, Z. Hu and Y. Wu, Investigations on the synthesis, crystal structure, linear-and nonlinear-optical properties of the zinc germanate $Rb_2ZnGe_2O_6$, *Inorg. Chem.*, 2021, **61**, 706–712.

42 J. Jiao, F. Liang, C. Li, T. Han, W. Zhao, Y. She, N. Ye, Z. Hu and Y. Wu, Shedding light on the structure and characterization of $K_2ZnGe_2O_6$: A phase-matchable nonlinear optical crystal, *Inorg. Chem.*, 2022, **61**, 11471–11477.

43 Z. Jia, X. Jiang, Z. Lin and M. Xia, $PbTeGeO_6$: polar rosiaite-type germanate featuring a two dimensional layered structure, *Dalton Trans.*, 2018, **47**, 16388–16392.

44 J. Yu, B. Zhang, X. Zhang, Y. Wang, K. Wu and M. H. Lee, Finding optimal mid-infrared nonlinear optical materials in germanates by first-principles high-throughput screening and experimental verification, *ACS Appl. Mater. Interfaces*, 2020, **12**, 45023–45035.

45 K. Chen, C. Lin, J. Chen, G. Yang, H. Tian, M. Luo, T. Yan, Z. Hu, J. Wang, Y. Wu, N. Ye and G. Peng, Intense d-p hybridization in Nb_3O_{15} tripolymer induced the largest second harmonic generation response and birefringence in germanates, *Angew. Chem.*, 2023, **135**, e202217039.

46 J. Xu, H. Wu, H. Yu, W. Zhang, Z. Hu, J. Wang, Y. Wu and P. S. Halasyamani, $Li_2K_4TiOGe_4O_{12}$: A stable mid-infrared nonlinear optical material, *Chem. Mater.*, 2019, **32**, 906–912.

47 M. Xia, C. Tang and R. Li, $Rb_4Li_2TiOGe_4O_{12}$: A titanyl nonlinear optical material with the widest transparency range, *Angew. Chem.*, 2019, **131**, 18425–18428.

48 A. Bhim, W. Zhang, P. S. Halasyamani, J. Gopalakrishnan and S. Natarajan, New members of SHG active dugganite family, $A_3BC_3D_2O_{14}$ (A = Ba, Pb; B = Te, Sb; C = Al, Ga, Fe,

This journal is © the Partner Organisations 2023

Inorg. Chem. Front., 2023, **10**, 6869–6878 | **6877**

Zn; D = Si, Ge, P, V): synthesis, structure, and materials properties, *Inorg. Chem.*, 2019, **58**, 8560–8569.

49 K. C. Chen, C. S. Lin, S. Z. Zhang, G. Peng, Y. Chen, D. Zhao, H. X. Fan, S. D. Yang, X. Wen, M. Luo, Z. S. Lin and N. Ye, $A_3Te(Zn_2Ge)Ge_2O_{14}$ (A = Sr, Ba, and Pb): New langasite mid-infrared nonlinear optical materials by rational chemical substitution, *Chem. Mater.*, 2021, **33**, 6012–6017.

50 D. Wang, Y. Zhang, Q. Liu, B. Zhang, D. Yang and Y. Wang, Band gap modulation and nonlinear optical properties of quaternary tellurates Li_2GeTeO_6, *Dalton Trans.*, 2022, **51**, 8955–8959.

51 J. Xu, H. Wu, H. Yu, Z. Hu, J. Wang and Y. Wu, Syntheses, characterization and calculations of $Li_mA_nM_6O_{15}$ (A = Rb, Cs; M = Si, Ge; m +n = 6), *Sci. China Mater.*, 2020, **63**, 1769–1778.